Geophysical Prospecting, 2003, **51**, 369–379

Frequency-dependent anisotropy due to meso-scale fractures in the presence of equant porosity

Mark Chapman*

British Geological Survey, Murchison House, West Mains Road, Edinburgh EH9 3LA, UK

Received May 2002, revision accepted April 2003

ABSTRACT

Fractured rock is often modelled under the assumption of perfect fluid pressure equalization between the fractures and equant porosity. This is consistent with laboratory estimates of the characteristic squirt-flow frequency. However, these laboratory measurements are carried out on rock samples which do not contain large fractures. We consider coupled fluid motion on two scales: the grain scale which controls behaviour in laboratory experiments and the fracture scale. Our approach reproduces generally accepted results in the low- and high-frequency limits. Even under the assumption of a high squirt-flow frequency, we find that frequency-dependent anisotropy can occur in the seismic frequency band when larger fractures are present. Shear-wave splitting becomes dependent on frequency, with the size of the fractures playing a controlling role in the relationship. Strong anisotropic attenuation can occur in the seismic frequency band. The magnitude of the frequency dependence is influenced strongly by the extent of equant porosity. With these results, it becomes possible in principle to distinguish between fracture- and microcrack-induced anisotropy, or more ambitiously to measure a characteristic fracture length from seismic data.

INTRODUCTION

A great deal of interest exists in the development of models which can relate fracturing in rock to anisotropic seismic properties. The importance of the problem has been illustrated by the observation of strong sensitivity of shear-wave splitting to the saturating fluid published by van der Kolk, Guest and Potters (2001). Observations of frequency-dependent shear-wave splitting in VSP data have been presented by Chesnokov *et al.* (2001).

The classical attempts to solve the problem (Schoenberg 1980; Hudson 1980, 1981; Liu, Hudson and Pointer 2000, for a thorough review) were derived under the assumption that no exchange of fluid took place, either between the fractures themselves or between the fractures and the rock matrix. However, the importance of fluid exchange between different parts of the pore space during seismic wave propagation has long been recognized (Gassmann 1951; Biot 1956; Brown and Korringa 1975; Mavko and Nur 1975; O'Connell and Budiansky 1977). Thomsen (1995) showed the relevance of these ideas to the interpretation of seismic anisotropy. This work allowed for the transfer of fluid between fractures and 'equant porosity' in the rock matrix. Perfect pressure equalization, corresponding to a wave of very low frequency, was assumed. Such an effect was shown to increase greatly the amount of seismic anisotropy which a given fracture distribution would produce.

More recent models proposed by Hudson, Liu and Crampin (1996), Pointer, Liu and Hudson (2000) and Tod (2001) and the BOSK model of van der Kolk *et al.* (2001) have attempted to extend these ideas to the entire frequency range. Various geometries are considered, consisting of simple aligned fractures, distributions of fracture orientations or aligned fractures connected to equant porosity. The application of these models to the experiments on synthetic fractured rock of Rathore *et al.* (1995) has been described by Hudson, Pointer and Liu (2001). Reasonable qualitative agreement was achieved, but sample size issues prevented a definitive test of any theory.

*E-mail: m.chapman@bgs.ac.uk

Sonic and ultrasonic laboratory measurements are carried out on small, typically well-consolidated, rock samples. It is fair to describe such samples as unfractured. Certainly they are too small to contain the meso-scale fractures which we wish to model. They exhibit dispersion (Spencer 1981; Murphy 1985; Lucet 1989; Sothcott, McCann and O'Hara 2000), attenuation (Winkler 1985), stress-sensitivity (Nur 1971) and dependence on fluid saturation (Jones 1986). The explanation of this anelastic behaviour must be based on grain-scale effects.

However, when the fractures are removed from any of the models referred to above, what results is a linearly elastic material, in direct contradiction to observation. We argue that to model meso-scale fractures, we need to develop a theory in which at least two length scales are explicit: the grain scale and the characteristic length scale of the fractures.

Chapman, Zatsepin and Crampin (2002) gave a poroelastic theory which modelled the effects of squirt flow at the grain scale. Chapman (2001a,b) argued that this model was capable of explaining the experimental measurements of Sothcott *et al.* (2000), who considered the effect of changes in frequency, saturation and effective stress in sandstone samples. This paper represents an attempt to incorporate meso-scale anisotropic fracturing into this analysis, taking into account the interactions between the two scales.

DESCRIPTION OF THE MODEL

Chapman *et al.* (2002) considered the case of a pore space which consisted of a random isotropic collection of microcracks and spherical pores. The radius of each crack and pore was identified with the grain size. We wish now to introduce a set of aligned fractures, which have radii larger than the grain size.

For simplicity, we assume that the microcracks and fractures have a common aspect ratio which we denote by r. We now establish the notation,

$$c_{\mathrm{v}} = \frac{4}{3}\pi a^3 r, \tag{1}$$

$$p_{\mathrm{v}} = \frac{4}{3}\pi a^3, \tag{2}$$

$$f_{\mathrm{v}} = \frac{4}{3}\pi a_{\mathrm{f}}^3 r, \tag{3}$$

where c_{v}, p_{v} and f_{v} are the volumes of the individual cracks, pores and fractures, respectively, a is the radius of the cracks and pores and a_{f} the radius of the fractures.

Following Chapman *et al.* (2002) we fix a number N_{c} and partition the surface of the unit sphere into N_{c} elements of equal area. We consider the case of a collection of N_{c} cracks each with a different orientation corresponding to one of the elements of area. Later we will allow N_{c} to approach infinity to simulate a random isotropic crack distribution.

Let the volume fractions, or porosities, associated with the cracks, pores and fractures be ϕ_{c}, ϕ_{p} and ϕ_{f}, respectively. Then define

$$N_{\mathrm{p}} = \frac{\phi_{\mathrm{p}} N_{\mathrm{c}} r}{\phi_{\mathrm{c}}}, \tag{4}$$

$$N_{\mathrm{f}} = \frac{\phi_{\mathrm{f}}}{\phi_{\mathrm{c}}}\left(\frac{a}{a_{\mathrm{f}}}\right)^3 N_{\mathrm{c}}. \tag{5}$$

We now define a collection $\mathcal{C}$ consisting of the N_{c} microcracks, N_{p} pores and N_{f} fractures. The physical significance of $\mathcal{C}$ is that, under the assumption of a homogeneous distribution, a macroscopic volume of rock would be expected to contain cracks, pores and fractures in the same relative numbers as does $\mathcal{C}$. It remains to specify a model for the exchange of fluid amongst the elements of $\mathcal{C}$.

In the model of Chapman *et al.* (2002), fluid was exchanged between adjacent voids a and b due to pressure gradients according to the formula,

$$\partial_t m_a = \frac{\rho_0 k \varsigma}{\eta}(p_b - p_a), \tag{6}$$

where ρ_0 is the fluid density, k is the permeability, ς is the grain size, η the fluid viscosity, p_a the pressure in element a and m_a the fluid mass in element a. It was assumed that each element was connected to six other elements, and that the resulting flows could be added linearly.

In our case, since the fractures are larger than the cracks and pores they should be connected to more elements. We assume that the cracks and pores are connected to c_1 other elements while the fractures are connected to c_2 elements. We also assume that each crack and pore is connected to at most one fracture, and that fractures are not connected to other fractures. For this to be possible, we must ensure that the number of cracks and pores vastly exceeds the number of fractures, or explicitly,

$$c_2 N_{\mathrm{f}} < N, \tag{7}$$

where

$$N = N_{\mathrm{c}} + N_{\mathrm{p}}. \tag{8}$$

We introduce the notation,

$$E_{\mathrm{p}} = \frac{1}{N}\sum_{i=1}^{N_{\mathrm{c}}} E[p_i] + \frac{N_{\mathrm{p}}}{N} E[p^*], \tag{9}$$

where p_i denotes the pressure in a crack of orientation i and p^* is the expected pressure in a pore. Now the probability that any given crack or pore, i, is connected to a fracture is given by

$$P(i \text{ connected to a fracture}) = \frac{c_2 N_{\mathrm{f}}}{N}. \tag{10}$$

In the event that i is not connected to a fracture, the expected mass flow out of i is, as given by Chapman *et al.* (2002),

$$E[\partial_t m_i \mid i \text{ not connected to fracture}] = \frac{c_1 \rho_0 k\varsigma}{\eta}(E_{\mathrm{p}} - E[p_i]). \tag{11}$$

The expected mass flow out of a crack which is connected to a fracture, however, is given by

$$E[\partial_t m_i \mid i \text{ connected to fracture}] = \frac{\rho_0 k\varsigma}{\eta}\{(c_1 - 1)(E_{\mathrm{p}} - E[p_i]) + (E[f] - E[p_i])\}, \tag{12}$$

where f denotes the pressure in the fracture. It follows then that the expected mass flow from an arbitrary crack or pore i is given by

$$\partial_t m_i = \frac{\rho_0 k\varsigma}{\eta}\left\{\left(\frac{N - c_2 N_{\mathrm{f}}}{N}\right) c_1 (E_{\mathrm{p}} - p_i) + \frac{c_2 N_{\mathrm{f}}}{N}[(c_1 - 1)(E_{\mathrm{p}} - p_i) + (f - p_i)]\right\}, \tag{13}$$

where it is to be understood that every variable is an expectation. The mass flow from an individual fracture is given by

$$\partial_t m_{\mathrm{f}} = \frac{c_2 \rho_0 k\varsigma}{\eta}(E_{\mathrm{p}} - f). \tag{14}$$

With this arrangement, we find that

$$\sum_{j \in \mathcal{C}} \partial_t m_j = 0. \tag{15}$$

This means that mass is conserved throughout the elements of $\mathcal{C}$.

The mass in each element of pore space can be given in terms of the inclusion pressure and the applied stress. Following Chapman *et al.* (2002), we write for the fluid mass in a crack of orientation i,

$$\partial_t m_i = \frac{\rho_0 c_{\mathrm{v}}}{\sigma_{\mathrm{c}}}\partial_t[(1 + K_{\mathrm{c}})p_i - \sigma_i], \tag{16}$$

where p_i is the pressure in the crack, σ_i is the normal stress acting on the crack face, $\sigma_{\mathrm{c}} = \frac{\pi \mu r}{2(1-\nu)}$ and $K_{\mathrm{c}} = \sigma_{\mathrm{c}}/\kappa_{\mathrm{f}}$, μ being the shear modulus, ν the Poisson's ratio of the matrix material and κ_{f} the fluid bulk modulus. Denoting the mass in each pore by m^*, we have

$$\partial_t m^* = \frac{3\rho_0 p_{\mathrm{v}}}{4\mu}\partial_t\left[(1 + K_{\mathrm{p}})p^* - \frac{1-\nu}{1+\nu}\sigma_{ii}\right], \tag{17}$$

where $K_{\mathrm{p}} = \frac{4\mu}{3\kappa_{\mathrm{f}}}$. The mass in each fracture, m_{f}, is given by

$$\partial_t m_{\mathrm{f}} = \frac{\rho_0 f_{\mathrm{v}}}{\sigma_{\mathrm{c}}}\partial_t[(1 + K_{\mathrm{c}})f - \sigma_{\mathrm{f}}], \tag{18}$$

where σ_{f} is the normal stress acting on the fracture face.

We now proceed to solve for the pressures in terms of the applied stress field. From (13), we have

$$\partial_t(m_i - m^*) = \frac{\rho_0 k\varsigma c_1}{\eta}(p^* - p_i), \tag{19}$$

for all crack orientations, i. Writing

$$\frac{1}{\tau_{\mathrm{m}}} = \frac{\sigma_{\mathrm{c}} k\varsigma c_1}{c_{\mathrm{v}}\eta(1 + K_{\mathrm{c}})}, \tag{20}$$

$$\gamma = \frac{3p_{\mathrm{v}}\sigma_{\mathrm{c}}(1 + K_{\mathrm{p}})}{4\mu c_{\mathrm{v}}(1 + K_{\mathrm{c}})}, \tag{21}$$

$$\gamma' = \gamma\frac{1-\nu}{1+\nu}\frac{1}{1 + K_{\mathrm{p}}}, \tag{22}$$

equations (16) and (17) give, in the frequency domain,

$$p_i = \frac{1}{1 + \mathrm{i}\omega\tau_{\mathrm{m}}}\left[\frac{\mathrm{i}\omega\tau_{\mathrm{m}}}{(1 + K_{\mathrm{c}})}\sigma_i - \gamma'\mathrm{i}\omega\tau_{\mathrm{m}}\sigma_{ii} + (1 + \mathrm{i}\omega\gamma\tau_{\mathrm{m}})p^*\right]. \tag{23}$$

If we write

$$\langle p\rangle = \frac{1}{N_{\mathrm{c}}}\sum_{i=1}^{N_{\mathrm{c}}} p_i, \tag{24}$$

$$\tau_{\mathrm{f}} = \frac{f_{\mathrm{v}}\eta(1 + K_{\mathrm{c}})}{c_2\sigma_{\mathrm{c}} k\varsigma}, \tag{25}$$

$$\iota = \frac{N_{\mathrm{c}}}{N}, \tag{26}$$

then (14) gives

$$f = \frac{1}{1 + \mathrm{i}\omega\tau_{\mathrm{f}}}\left[\frac{\mathrm{i}\omega\tau_{\mathrm{f}}}{1 + K_{\mathrm{c}}}\sigma_{\mathrm{f}} + \iota\langle p\rangle + (1 - \iota)p^*\right]. \tag{27}$$

We now introduce the notation,

$$\beta = \frac{\iota\phi_{\mathrm{f}}}{\phi_{\mathrm{c}}}. \tag{28}$$

Equations (15), (23) and (27) now give

$$p^* = D_1\sigma_{ll} + D_2\sigma_{\mathrm{f}}, \tag{29}$$

where

$$D_1 = \left[(1-\iota)\gamma + \frac{(1-\iota)\beta}{1+\mathrm{i}\omega\tau_\mathrm{f}} + \left(\iota + \frac{\iota\beta}{1+\mathrm{i}\omega\tau_\mathrm{f}}\right)\left(\frac{1+\mathrm{i}\omega\gamma\tau_\mathrm{m}}{1+\mathrm{i}\omega\tau_\mathrm{m}}\right)\right]^{-1} \times \left[\frac{\iota}{3(1+K_\mathrm{c})} + (1-\iota)\gamma' - \frac{\mathrm{i}\omega\tau_\mathrm{m}}{1+\mathrm{i}\omega\tau_\mathrm{m}} \times \left(\frac{1}{3(1+K_\mathrm{c})} - \gamma'\right)\left(\iota + \frac{\iota\beta}{1+\mathrm{i}\omega\tau_\mathrm{f}}\right)\right], \tag{30}$$

$$D_2 = \left[(1-\iota)\gamma + \frac{(1-\iota)\beta}{1+\mathrm{i}\omega\tau_\mathrm{f}} + \left(\iota + \frac{\iota\beta}{1+\mathrm{i}\omega\tau_\mathrm{f}}\right)\left(\frac{1+\mathrm{i}\omega\gamma\tau_\mathrm{m}}{1+\mathrm{i}\omega\tau_\mathrm{m}}\right)\right]^{-1} \times \left(\frac{\beta}{(1+K_\mathrm{c})(1+\mathrm{i}\omega\tau_\mathrm{f})}\right). \tag{31}$$

With this result, (23) may be made to read

$$p_i = G_1\sigma_i + G_2\sigma_{ii} + G_3\sigma_\mathrm{f}, \tag{32}$$

where

$$G_1 = \frac{\mathrm{i}\omega\tau_\mathrm{m}}{(1+K_\mathrm{c})(1+\mathrm{i}\omega\tau_\mathrm{m})}, \tag{33}$$

$$G_2 = \frac{1+\mathrm{i}\omega\gamma\tau_\mathrm{m}}{1+\mathrm{i}\omega\tau_\mathrm{m}} D_1 - \frac{\mathrm{i}\omega\tau_\mathrm{m}\gamma'}{1+\mathrm{i}\omega\tau_\mathrm{m}}, \tag{34}$$

$$G_3 = \frac{1+\mathrm{i}\omega\gamma\tau_\mathrm{m}}{1+\mathrm{i}\omega\tau_\mathrm{m}} D_2. \tag{35}$$

Meanwhile, (27) can be written as

$$f = F_1\sigma_{ii} + F_2\sigma_\mathrm{f}, \tag{36}$$

where

$$F_1 = \frac{1}{1+\mathrm{i}\omega\tau_\mathrm{f}}\left[\frac{1+\mathrm{i}\omega\gamma\tau_\mathrm{m}}{1+\mathrm{i}\omega\tau_\mathrm{m}}\iota D_1 + (1-\iota)D_1 + \frac{\mathrm{i}\iota\omega\tau_\mathrm{m}}{1+\mathrm{i}\omega\tau_\mathrm{m}}\left(\frac{1}{3(1+K_\mathrm{c})} - \gamma'\right)\right], \tag{37}$$

$$F_2 = \frac{1}{1+\mathrm{i}\omega\tau_\mathrm{f}}\left[\frac{\mathrm{i}\omega\tau_\mathrm{f}}{1+K_\mathrm{c}} + \iota\frac{1+\mathrm{i}\omega\gamma\tau_\mathrm{m}}{1+\mathrm{i}\omega\tau_\mathrm{m}} D_2 + (1-\iota)D_2\right]. \tag{38}$$

Equations (29), (32) and (36) give the time-dependent response of the pressures in the various inclusions to an imposed stress field. Having established these relationships, we now proceed to the calculation of the effective elastic tensor. Eshelby's (1957) interaction energy approach for the calculation of the effective elastic constants of a material with embedded inclusions gives the formula,

$$C_{ijkl}\epsilon^0_{ij}\epsilon^0_{kl} = C^\mathrm{m}_{ijkl}\epsilon^0_{ij}\epsilon^0_{kl} - \sum_n \phi_n\left(\epsilon^\mathrm{inc}_{ij}\sigma^0_{ij} - \sigma^\mathrm{inc}_{ij}\epsilon^0_{ij}\right), \tag{39}$$

where C is the effective elastic tensor, C^m is the elastic tensor of the rock matrix, ϵ^0 is the applied strain field, ϕ_n is the volume fraction of the nth inclusion and σ^inc and ϵ^inc are the stress and strain fields inside each inclusion. Equation (39) is valid for a dilute concentration of inclusions. We introduce Cartesian coordinates in which the x_3-axis is aligned with the fracture normal direction.

To use (39) we need to know the states of stress and strain inside each inclusion. These may be calculated from our knowledge of the pressure fields. Our strategy is therefore as follows: We will choose appropriate values of ϵ^0 to isolate appropriate components of the effective elastic tensor on the left-hand side of (39). We will then calculate ϵ^inc and σ^inc from (29), (32) and (39), which will yield an explicit formula for the relevant component of the elastic tensor. We first choose

$$\epsilon^0_{ij} = \begin{bmatrix} 1 & 0 & 0 \\ 0 & 0 & 0 \\ 0 & 0 & 0 \end{bmatrix} s(t), \tag{40}$$

where $s(t)$ is a harmonic function. Equation (39) gives

$$C_{1111} = C^\mathrm{m}_{1111} - \frac{1}{[s(t)]^2}\sum_n \phi_n\left(\epsilon^\mathrm{inc}_{ij}\sigma^0_{ij} - \sigma^\mathrm{inc}_{ij}\epsilon^0_{ij}\right). \tag{41}$$

We find that

$$\sigma^0_{ij} = \begin{bmatrix} \lambda+2\mu & 0 & 0 \\ 0 & \lambda & 0 \\ 0 & 0 & \lambda \end{bmatrix} s(t) \tag{42}$$

and

$$\sigma^\mathrm{inc}_{ij} = \begin{bmatrix} p & 0 & 0 \\ 0 & p & 0 \\ 0 & 0 & p \end{bmatrix}, \tag{43}$$

where p is the pressure in any given inclusion. The strain in each inclusion is given by the formula (Zatsepin and Crampin 1997),

$$\epsilon^\mathrm{inc} = (I-S)^{-1}C^{-1}(\sigma^0 - CSC^{-1}p\delta), \tag{44}$$

where S is the Eshelby tensor (Eshelby 1957) associated with each inclusion.

For a crack of orientation i, we have

$$\epsilon^\mathrm{inc}_{ij} = \begin{bmatrix} (\sigma_i - p_i)/\sigma_\mathrm{c} & T\epsilon^i_{12} & T\epsilon^i_{13} \\ T\epsilon^i_{21} & 0 & 0 \\ T\epsilon^i_{31} & 0 & 0 \end{bmatrix}, \tag{45}$$

where ϵ^i_{jk} is the jkth component of strain acting on the crack face and

$$T = \frac{4(1-\nu)}{(2-\nu)\pi r}. \tag{46}$$

Following Chapman *et al.* (2002), we find

$$\sum_{\text{cracks}} \phi_i \left(\epsilon_{ij}^{\text{inc}} \sigma_{ij}^0 - \sigma_{ij}^{\text{inc}} \epsilon_{ij}^0\right) = \phi_c \left[\frac{L_2}{\sigma_c} + \frac{8}{15}\frac{(1-\nu)\mu}{(2-\nu)\pi r} - \left(\frac{L_2}{\sigma_c} + \kappa\right) G_1 - \left(\frac{3\kappa^2}{\sigma_c} + 3\kappa\right) G_2 - \left(\frac{\lambda\kappa}{\sigma_c} + \lambda\right) G_3\right], \tag{47}$$

where $\kappa = \lambda + \frac{2}{3}\mu$ and

$$L_2 = \lambda^2 + \frac{4}{3}\lambda\mu + \frac{4}{5}\mu^2. \tag{48}$$

Now, the same technique gives

$$\sum_{\text{pores}} \phi_i \left(\epsilon_{ij}^{\text{inc}} \sigma_{ij}^0 - \sigma_{ij}^{\text{inc}} \epsilon_{ij}^0\right) = \phi_p \left[\frac{3}{4\mu}\frac{1-\nu}{1+\nu}\left(3\lambda^2 + 4\lambda\mu + \frac{36+20\nu}{7-5\nu}\mu^2\right) - \left(1 + \frac{3\kappa}{4\mu}\right)(3\kappa D_1 + \lambda D_2)\right], \tag{49}$$

and finally

$$\sum_{\text{fractures}} \phi_i \left(\epsilon_{ij}^{\text{inc}} \sigma_{ij}^0 - \sigma_{ij}^{\text{inc}} \epsilon_{ij}^0\right) = \phi_f \left[\frac{\lambda^2}{\sigma_c} - \left(\frac{3\lambda\kappa}{\sigma_c} + 3\kappa\right) F_1 - \left(\frac{\lambda^2}{\sigma_c} + \lambda\right) F_2\right]. \tag{50}$$

Equation (41) now gives

$$\begin{aligned} C_{1111} = (\lambda + 2\mu) &- \phi_c \left[\frac{L_2}{\sigma_c} + \frac{32}{15}\frac{1-\nu}{(2-\nu)\pi r}\mu - \left(\frac{L_2}{\sigma_c} + \kappa\right) G_1 - \left(\frac{3\kappa^2}{\sigma_c} + 3\kappa\right) G_2 - \left(\frac{\lambda\kappa}{\sigma_c} + \lambda\right) G_3\right] \\ &- \phi_p \left[\frac{3}{4\mu}\frac{1-\nu}{1+\nu}\left(3\lambda^2 + 4\lambda\mu + \frac{36+20\nu}{7-5\nu}\mu^2\right) - \left(1 + \frac{3\kappa}{4\mu}\right)(3\kappa D_1 + \lambda D_2)\right] \\ &- \phi_f \left[\frac{\lambda^2}{\sigma_c} - \left(\frac{3\lambda\kappa}{\sigma_c} + 3\kappa\right) F_1 - \left(\frac{\lambda^2}{\sigma_c} + \lambda\right) F_2\right]. \end{aligned} \tag{51}$$

The expression for C_{3333} may be calculated by the same procedure, replacing the condition $\sigma_f = \lambda s(t)$ with $\sigma_f = (\lambda + 2\mu)s(t)$:

$$\begin{aligned} C_{3333} = (\lambda + 2\mu) &- \phi_c \left[\frac{L_2}{\sigma_c} + \frac{32}{15}\frac{1-\nu}{(2-\nu)\pi r}\mu - \left(\frac{L_2}{\sigma_c} + \kappa\right) G_1 - \left(\frac{3\kappa^2}{\sigma_c} + 3\kappa\right) G_2 - \left(\frac{(\lambda+2\mu)\kappa}{\sigma_c} + \lambda + 2\mu\right) G_3\right] \\ &- \phi_p \left[\frac{3}{4\mu}\frac{1-\nu}{1+\nu}\left(3\lambda^2 + 4\lambda\mu + \frac{36+20\nu}{7-5\nu}\mu^2\right) - \left(1 + \frac{3\kappa}{4\mu}\right)(3\kappa D_1 + (\lambda+2\mu) D_2)\right] \\ &- \phi_f \left[\frac{(\lambda+2\mu)^2}{\sigma_c} - \left(\frac{3(\lambda+2\mu)\kappa}{\sigma_c} + 3\kappa\right) F_1 - \left(\frac{(\lambda+2\mu)^2}{\sigma_c} + \lambda + 2\mu\right) F_2\right]. \end{aligned} \tag{52}$$

If we now choose

$$\epsilon_{ij}^0 = \begin{bmatrix} 0 & 0 & 1 \\ 0 & 0 & 0 \\ 1 & 0 & 0 \end{bmatrix} s(t), \tag{53}$$

then we find

$$\begin{aligned} C_{2323} = \mu &- \phi_c \left[\frac{4}{15}\frac{\mu^2}{\sigma_c}(1 - G_1) + \frac{8}{5}\frac{1-\nu}{(2-\nu)\pi r}\mu\right] \\ &- 15\phi_p \frac{1-\nu}{7-5\nu}\mu - \phi_f \frac{4(1-\nu)}{(2-\nu)\pi r}\mu. \end{aligned} \tag{54}$$

Choosing now

$$\epsilon_{ij}^0 = \begin{bmatrix} 1 & 0 & 0 \\ 0 & 1 & 0 \\ 0 & 0 & 0 \end{bmatrix} s(t), \tag{55}$$

we find

$$\begin{aligned} 2(C_{1111} + C_{1122}) = 4(\lambda + \mu) &- \phi_c \left[\frac{L_3}{\sigma_c} + \frac{32}{15}\frac{1-\nu}{(2-\nu)\pi r}\mu - \left(\frac{L_3}{\sigma_c} + 4\kappa\right) G_1 - 12\kappa\left(1 + \frac{\kappa}{\sigma_c}\right) G_2 - 4\lambda\left(1 + \frac{\kappa}{\sigma_c}\right) G_3\right] \\ &- \phi_p \left[\frac{3}{4\mu}\frac{1-\nu}{1+\nu}\left(12\lambda^2 + 16\lambda\mu + \frac{64}{7-5\nu}\mu^2\right) - \left(2 + \frac{3\kappa}{2\mu}\right)(6\kappa D_1 + 2\lambda D_2)\right] \\ &- \phi_f \left[\frac{4\lambda^2}{\sigma_c} - 12\kappa\left(1 + \frac{\lambda}{\sigma_c}\right) F_1 - 4\lambda\left(1 + \frac{\lambda}{\sigma_c}\right) F_2\right], \end{aligned} \tag{56}$$

where

$$L_3 = 4\left(\lambda^2 + \frac{4}{3}\lambda\mu + \frac{8}{15}\mu^2\right). \tag{57}$$

With this equation it is possible to calculate C_{1122} directly from (51). Introducing the notation,

$$L_4 = \lambda^2 + \frac{4}{3}\lambda\mu + \frac{4}{15}\mu^2, \tag{58}$$

we have

$$\begin{aligned} C_{1122} = \lambda &- \phi_c\left[\frac{L_4}{\sigma_c} - \frac{16}{15}\frac{1-\nu}{(2-\nu)\pi r}\mu - \left(\frac{L_4}{\sigma_c} + \kappa\right)G_1\right. \\ &\left. - \left(\frac{3\kappa^2}{\sigma_c} + 3\kappa\right)G_2 - \left(\frac{\lambda\kappa}{\sigma_c} + \lambda\right)G_3\right] \\ &- \phi_p\left[\frac{3}{4\mu}\frac{1-\nu}{1+\nu}\left(3\lambda^2 + 4\lambda\mu - \frac{4(1+5\nu)}{7-5\nu}\mu^2\right)\right. \\ &\left. - \left(1 + \frac{3\kappa}{4\mu}\right)(3\kappa D_1 + \lambda D_2)\right] \\ &- \phi_f\left[\frac{\lambda^2}{\sigma_c} - 3\kappa\left(1 + \frac{\lambda}{\sigma_c}\right)F_1 - \lambda\left(1 + \frac{\lambda}{\sigma_c}\right)F_2\right]. \end{aligned} \tag{59}$$

By similar means, it may be shown that

$$\begin{aligned} &C_{1111} + C_{3333} + 2C_{1133} \\ &= 4(\lambda+\mu) - \phi_c\left[\frac{L_3}{\sigma_c} + \frac{32}{15}\frac{1-\nu}{(2-\nu)\pi r}\mu - \left(\frac{L_3}{\sigma_c} + 4\kappa\right)G_1\right. \\ &\quad \left. - 12\kappa\left(1 + \frac{\kappa}{\sigma_c}\right)G_2 - 4(\lambda+\mu)\left(1 + \frac{\kappa}{\sigma_c}\right)G_3\right] \\ &\quad - \phi_p\left[\frac{3}{4\mu}\frac{1-\nu}{1+\nu}\left(12\lambda^2 + 16\lambda\mu + \frac{64}{7-5\nu}\mu^2\right)\right. \\ &\quad \left. - \left(2 + \frac{3\kappa}{2\mu}\right)(6\kappa D_1 + 2(\lambda+\mu)D_2)\right] \\ &\quad - \phi_f\left[\frac{4(\lambda+\mu)^2}{\sigma_c} - 12\kappa\left(1 + \frac{\lambda+\mu}{\sigma_c}\right)F_1\right. \\ &\quad \left. - \left(\frac{4(\lambda+\mu)^2}{\sigma_c} + 4\lambda + 4\mu\right)F_2\right], \end{aligned} \tag{60}$$

and C_{1133}, calculated from (51) and (52), is given by

$$\begin{aligned} C_{1133} = \lambda &- \phi_c\left[\frac{L_4}{\sigma_c} - \frac{16}{15}\frac{1-\nu}{(2-\nu)\pi r}\mu - \left(\frac{L_4}{\sigma_c} + \kappa\right)G_1\right. \\ &\left. - 3\kappa\left(1 + \frac{\kappa}{\sigma_c}\right)G_2 - (\lambda+\mu)\left(1 + \frac{\kappa}{\sigma_c}\right)G_3\right] \\ &- \phi_p\left[\frac{3}{4\mu}\frac{1-\nu}{1+\nu}\left(3\lambda^2 + 4\lambda\mu + \frac{4(1+5\nu)}{7-5\nu}\mu^2\right)\right. \\ &\left. - \left(1 + \frac{3\kappa}{4\mu}\right)(3\kappa D_1 + (\lambda+\mu)D_2)\right] \\ &- \phi_f\left[\frac{\lambda(\lambda+2\mu)}{\sigma_c} - 3\kappa\left(1 + \frac{\lambda+\mu}{\sigma_c}\right)F_1\right. \\ &\left. - \left(\lambda + \mu + \frac{\lambda(\lambda+\mu)}{\sigma_c}\right)F_2\right]. \end{aligned} \tag{61}$$

This completes the calculation of the frequency-dependent, anisotropic, elastic tensor.

An important feature of the modelling is the similarity of the parametrization to that of the model of Chapman *et al.* (2002). Only the four parameters, ϕ_f, β, τ_f and a_f, in the analysis do not appear in the work of Chapman *et al.* (2002). The determination of the other parameters has been discussed in detail by Chapman *et al.* (2002). It was suggested that γ could be estimated with the approximation,

$$\gamma = \frac{3\pi}{8(1-\nu)}\left(1 + \frac{4}{3}\frac{\rho_s}{\rho_f}\left(\frac{V_s}{V_f}\right)^2\right), \tag{62}$$

where ρ_f and ρ_s are the densities of the fluid and solid respectively, V_s is a representative shear-wave velocity and V_f is the acoustic velocity in the fluid. If we assume that the crack aspect ratio is small enough that $K_c \ll 1$ (very thin cracks in the terminology of Thomsen (1995)), then the model can be expressed with dependence only on crack density, $\epsilon = \frac{3\phi_c}{4\pi r}$, and ι is approximated as

$$\iota = \frac{\frac{4}{3}\pi\epsilon}{\frac{4}{3}\pi\epsilon + \phi_p}. \tag{63}$$

Similar arguments lead to the approximation,

$$\beta = \frac{\frac{4}{3}\pi\epsilon_f}{\frac{4}{3}\pi\epsilon + \phi_p}, \tag{64}$$

where $\epsilon_f = \frac{3\phi_f}{4\pi r}$ is the fracture density.

Since f_v, c_v and σ_c are all proportional to the aspect ratio, (20) and (25) give

$$\frac{\tau_f}{\tau_m} = \frac{a_f^3}{a^3}\frac{c_1}{c_2}. \tag{65}$$

Clearly the connection numbers c_1 and c_2 must depend on the size of the cracks and fractures. Since the flow of fluid from an inclusion will be an integral over surface area, we suggest that the natural scaling is

$$c_1 \sim a^2, \tag{66}$$

$$c_2 \sim a_f^2, \tag{67}$$

whereupon, identifying the pore and microcrack radii with the grain size ς, we find

$$\tau_f = \left(\frac{a_f}{\varsigma}\right)\tau_m. \tag{68}$$

This implies that the effect of the fractures can be described with only two additional parameters: the fracture density ϵ_f and the fracture radius a_f. From (68) the important interpretation can be made that the time scale for pressure equalization depends on the fracture radius; larger fractures lead to lower characteristic frequencies for squirt-flow effects.

NUMERICAL RESULTS

To generate some numerical results, we will choose, somewhat arbitrarily, a set of parameters. Our reference elastic moduli will be $\lambda = \mu = 1.75 \times 10^{10}$ Pa, and the density will be 2300 kg/m^3. Crack density will be 0.1 and a 10% porosity will be assumed unless otherwise stated. To simulate water-saturated rock, we follow Chapman (2001a) and assume $\gamma = 10$ and $\gamma' = 1$. The aspect ratio is considered to be small enough that K_c may be ignored.

It is often stated (Thomsen 1995) that, allowing for variability in rock and fluid type, the squirt-flow frequency usually lies somewhere between the sonic and ultrasonic frequency ranges. This understanding results from an analysis of laboratory rock-physics data (Murphy 1985; Mavko and Jizba 1991; Sothcott *et al.* 2000). It should be noted that such experiments are performed on small rock samples which by definition contain features only at the grain scale. We identify this 'microstructural' squirt-flow frequency with $1/\tau_m$. Indeed, Chapman (2001a) deduced the value $\tau_m = 2 \times 10^{-5}$ s for the water-saturated sandstone used in the experimental work of Sothcott *et al.* (2000), and we shall use this value in the current study.

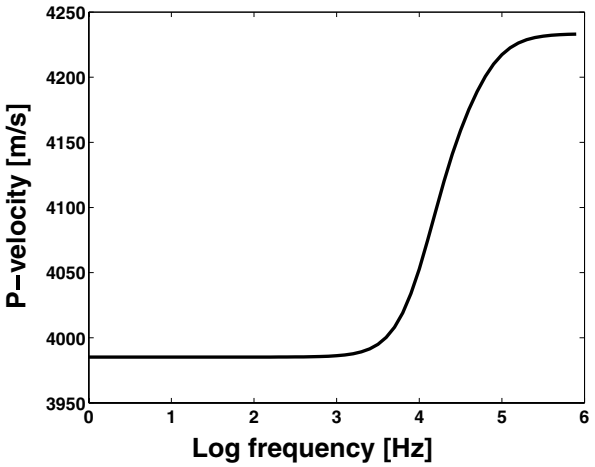

Figure 1 P-wave dispersion curve for the unfractured rock.

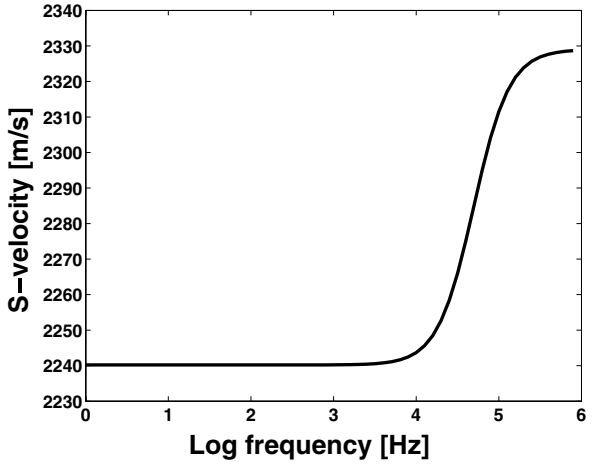

Figure 2 S-wave dispersion curve for the unfractured rock.

In the absence of fractures, the rock is isotropic and the dispersion curves for P- and S-waves are as given in Figs 1 and 2. It can be seen that the dispersion takes place over a limited frequency band, roughly between 1 kHz and 100 kHz. The model predicts that there is no dispersion over the seismic frequency band.

This situation changes with the introduction of a fracture set. We introduce a set of fractures with density 0.05 and a length of 10 cm. The rock is now transversely isotropic. In Fig. 3, we show the dispersion curves for the qP-wave for propagation parallel and normal to the fractures. As might be expected, the qP-wave travelling at right angles to the fracture normals is unaffected by the presence of the fractures. The situation for the wave travelling parallel to the fracture normals is different. At low frequency this qP-velocity is substantially lower than that for propagation at 90°. Dispersion

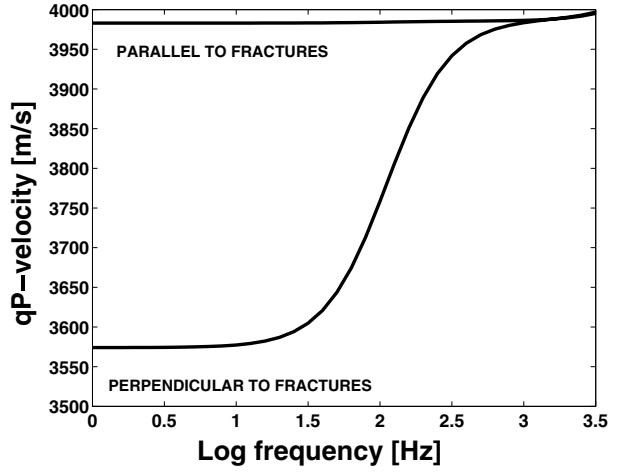

Figure 3 Dispersion curves for qP-waves travelling parallel and perpendicular to the fractures.

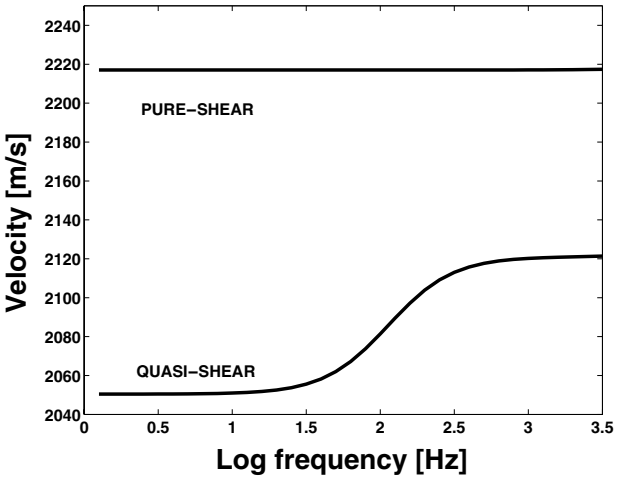

Figure 4 Dispersion curves for quasi- and pure-shear modes propagating at 70° to the fracture normal.

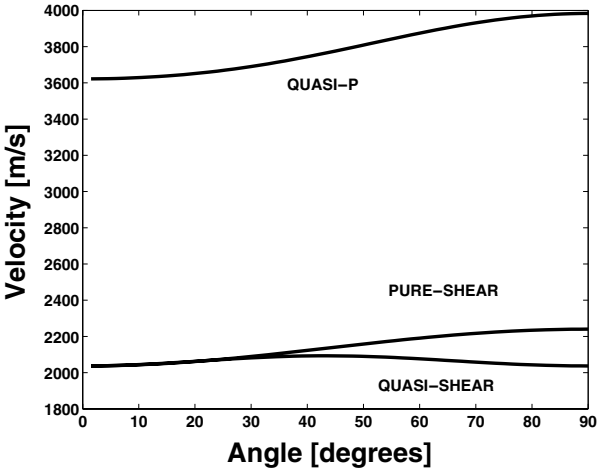

Figure 5 Angular variation of velocity for quasi-P, quasi-shear and pure-shear waves for a frequency of 40 Hz and a fracture size of 10 cm.

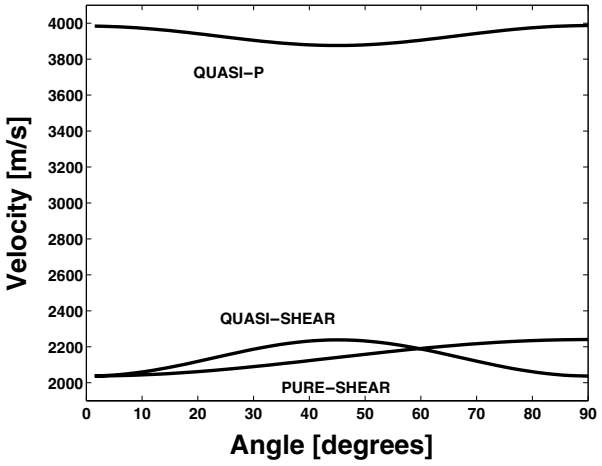

Figure 6 Angular variation of velocity for quasi-P, quasi-shear and pure-shear waves for a frequency of 1 kHz and a fracture size of 10 cm.

occurs over the 0–1 kHz range. This is an important feature of the fracture modelling; the existence of larger fractures introduces additional dispersion at lower frequency ranges than those over which the 'microstructural' dispersion occurs. The larger the size of the fractures, the lower is the relevant frequency band. We notice that for a frequency of 1 kHz the two qP-velocities become equal. This agrees with the prediction of Hudson (1981) who showed that when thin cracks are considered to be isolated from each other with respect to fluid flow the qP-velocities parallel and perpendicular to the cracks should be the same.

Figure 4 shows the dispersion curves for the shear waves polarized parallel and perpendicular to the fractures propagating at an angle of 45°. The pure-shear wave does not compress the fractures, so it shows no dispersion beneath the microstructural squirt frequency. The quasi-shear wave, however, does induce fluid flow between the fractures and the microcracks and pores. Consequently, this velocity increases with frequency.

The importance of frequency to the anisotropic behaviour is illustrated in Figs 5 and 6. These give quasi-P, quasi-shear and pure-shear velocities against angle of propagation, θ, for frequencies of 40 Hz (Fig. 5) and 1 kHz (Fig. 6). It is noticeable that the quasi-P velocity exhibits cos 4θ variation at 1 kHz, but cos 2θ variation at 40 Hz. This is consistent with the analysis of Thomsen (1995).

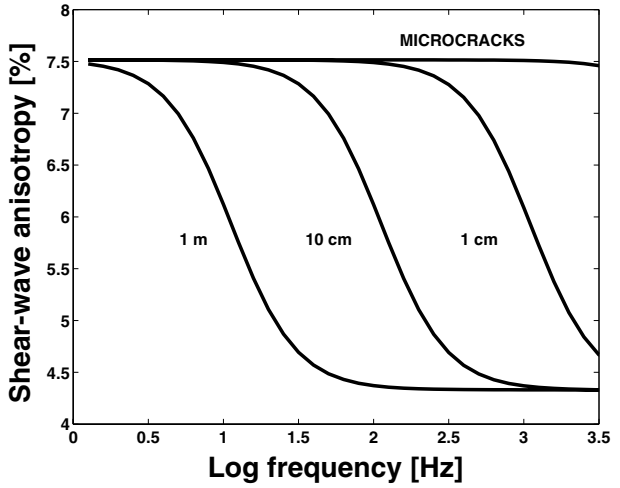

Figure 7 Shear-wave anisotropy as a function of frequency for various fracture sizes, with 10% equant porosity and a crack density of 0.1. Propagation is at 70° to the fracture normal.

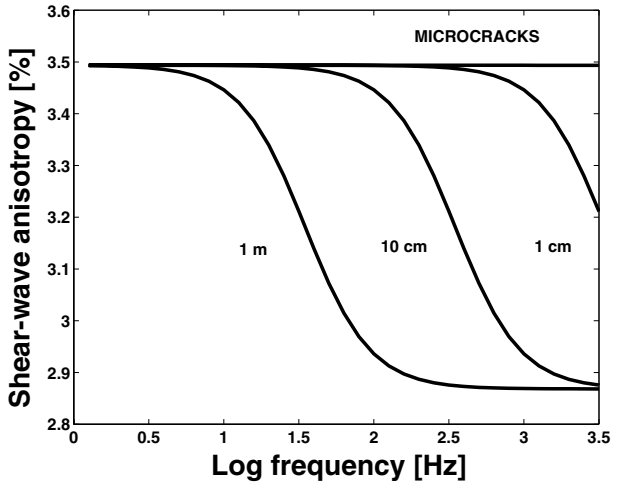

Figure 8 Shear-wave anisotropy as a function of frequency for various fracture sizes, with 0% equant porosity and a crack density of 0.02. Propagation is at 70° to the fracture normal.

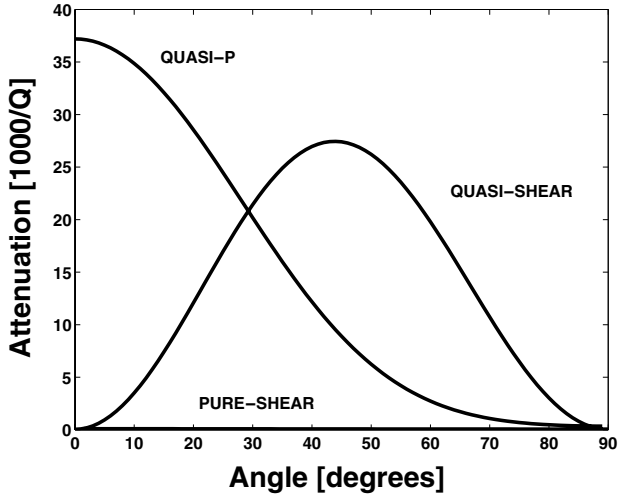

Figure 9 Angular variation of attenuation for qP-, qS- and S-waves for a frequency of 40 Hz and a fracture size of 10 cm.

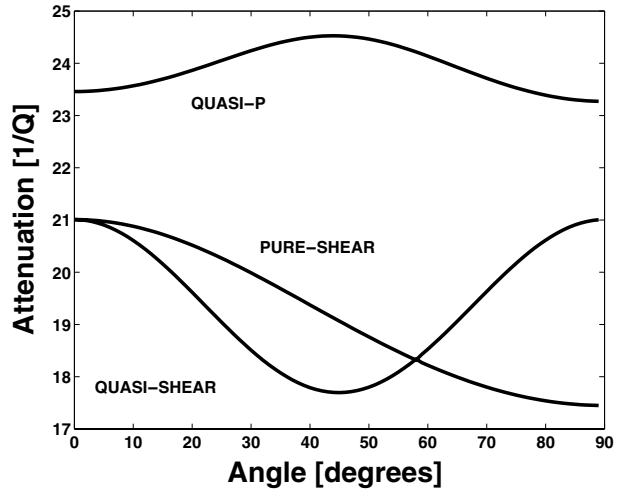

Figure 10 Angular dependence of attenuation for qP-, qS- and S-waves for a frequency of 3 kHz and a fracture size of 10 cm.

Figure 7 shows the relationship between shear-wave anisotropy, defined to be $100(S1-S2)/S1$ where $S1$ is the faster shear-wave velocity and $S2$ the slower velocity, and frequency for various fracture sizes from 200 μm microcracks up to 1 m fractures. Propagation is at 70° to the fracture normals. We note that the percentage anisotropy falls with increasing frequency, with the region over which the fall takes place depending on the length of the fractures. Figure 8 shows the same relationship, but this time for the case where the porosity is reduced from 10% to 0% and the crack density is reduced from 0.1 to 0.02. It can be seen that while the form of the relationship is similar to that in Fig. 8, the magnitude of the anisotropy is sharply decreased. This is an example of the equant porosity effect (Thomsen 1995). The pores, while themselves being isotropic, permit fluid to flow out of the anisotropic fractures, making them more compliant and therefore increasing the anisotropy of the whole medium.

In Figs 9 and 10, we plot the attenuation as a function of angle for frequencies of 40 Hz and 3 kHz, respectively. At 40 Hz, the attenuation of both the quasi-P and quasi-shear wave is significant, with the pure-shear wave not being strongly attenuated. We suspect that the lack of attenuation at 90° is an artefact introduced by the fact that the cracks are

perfectly aligned. Tod (2001) has discussed this effect and shown how it can be rectified by the introduction of a 'nearly aligned' crack set. At 3 kHz, all three waves are attenuated. This analysis shows how, in the presence of more than one length scale, the concept of squirt flow can explain attenuation across a very wide frequency band.

DISCUSSION

This paper underlines the significance of the work of Thomsen (1995), who demonstrated the importance of the concepts of pressure communication and equant porosity to the interpretation of seismic anisotropy. Nevertheless, our analysis suggests that in the presence of meso-scale fractures it may not be safe to assume that seismic frequencies represent the zero-frequency limit.

Even under the assumption that the squirt-flow frequency as deduced from laboratory measurements is above the sonic range, we demonstrate that substantial dispersion and attenuation can exist in the seismic range. In particular, a frequency-dependent anisotropic response may be expected.

The scale length of the fractures plays a key role in the analysis. This presents a potential method for discriminating between microcrack- and fault-induced anisotropy. More ambitiously, with sufficient local calibration, it may be possible to measure a characteristic fracture scale from seismic data.

Our analysis suggests a two-stage approach to the upscaling of laboratory measurements. Undoubtedly, unfractured rock is intrinsically dispersive, and this accounts for some of the difference between laboratory measurements and field observations. However, *in situ* rocks also contain larger fractures and these introduce additional dispersion. All but two of the parameters which appear in the theory, the fracture density and radius, have previously been measured from laboratory data (Chapman 2001a). This means that we can, at least in principle, first correct laboratory measurements for intrinsic dispersion and then study the effects of fracturing.

We have performed numerical tests which confirm the consistency of the low-frequency behaviour with the work of Brown and Korringa (1975). It is apparent that the first-order formulae of Hudson (1981) are contained as the high-frequency, zero-porosity limit. This consistency strengthens our confidence in the robustness of the approach.

Needless to say, the assumptions that the fractures are perfectly aligned and of the same size are not likely to be correct in practice. Tod (2001) has shown that a perfectly aligned fracture set can behave differently from a 'nearly aligned' fracture set. We consider the complete lack of dispersion of the pure-shear wave and the qP-wave at 90° over the seismic frequency range to be artefacts introduced by this assumption, although we expect these dispersions will still be small. It is possible that when a range of fracture sizes are present the increase in the velocities with frequency will be less abrupt than is suggested by the current model. Future work will address these limitations.

CONCLUSIONS

We demonstrate that, in the presence of larger fractures, a frequency-dependent anisotropic response may be expected in the seismic band, even when the 'squirt-flow frequency' lies above the sonic band. Previous work (Thomsen 1995) has argued that the qP-velocity should exhibit $\cos 2\theta$ dependence on angle at low frequency and $\cos 4\theta$ dependence at high frequency. This study confirms this conclusion, and gives an explicit frequency dependence for the transition. The model suggests a relationship between shear-wave splitting and frequency, with the fracture size playing a key role. A feature of the predicted behaviour is a link between fracturing and strong attenuation anisotropy in the seismic band. The magnitude of these effects increases with the equant porosity.

ACKNOWLEDGEMENTS

The author is grateful to Sonja Maultzsch, Sergei Zatsepin, Enru Liu, Xiang-Yang Li and Simon Tod for many conversations on this topic. Constructive reviews by Boris Gurevich and an anonymous reviewer improved the manuscript. This work is supported by the NERC thematic project 'Understanding the micro-to-macro behaviour of rock fluid systems' under contract GST022305. The work is presented with the approval of the Executive Director of the British Geological Survey (NERC).

REFERENCES

Biot M.A. 1956. Theory of propagation of elastic waves in fluid-saturated porous solid, I. Low frequency range, II. Higher frequency range. *Journal of the Acoustical Society of America* **28**, 168–191.

Brown R. and Korringa J. 1975. On the dependence of the elastic properties of a porous rock on the compressibility of the pore fluid. *Geophysics* **40**, 608–616.

Chapman M. 2001a. *Modelling the wide-band laboratory response of rock samples to fluid and pressure changes*. PhD thesis, University of Edinburgh.

Chapman M. 2001b. The dynamic fluid substitution problem. 71st SEG Meeting, San Antonio, Texas, USA, Expanded Abstracts, 1708–1711.

Chapman M., Zatsepin S.V. and Crampin S. 2002. Derivation of a microstructural poroelastic model. *Geophysical Journal International* **151**, 427–451.

Chesnokov E.M., Queen J.H., Vichorev A., Lynn H.B., Hooper J., Bayuk I., Castagna J. and Roy B. 2001. Frequency-dependent anisotropy. 71st SEG Meeting, San Antonio, Texas, USA, Expanded Abstracts, 2120–2123.

Eshelby J.D. 1957. The determination of the elastic field of an ellipsoidal inclusion, and related problems. *Proceedings of the Royal Society of London A* **241**, 376–396.

Gassmann F. 1951. Über die Elastizität poröser Medien. *Vier. der Natur. Gesellschaft in Zürich* **96**, 1–23.

Hudson J.A. 1980. Overall properties of a cracked solid. *Mathematical Proceedings of the Cambridge Philosophical Society* **88**, 371–384.

Hudson J.A. 1981. Wave speeds and attenuation of elastic waves in material containing cracks. *Geophysical Journal of the Royal Astronomical Society* **64**, 133–150.

Hudson J.A., Liu E. and Crampin S. 1996. The mechanical properties of materials containing interconnected cracks and pores. *Geophysical Journal International* **124**, 105–112.

Hudson J.A., Pointer T. and Liu E. 2001. Effective-medium theories for fluid-saturated materials with aligned cracks. *Geophysical Prospecting* **49**, 509–522.

Jones T. 1986. Pore fluids and frequency-dependent wave propagation in rocks. *Geophysics* **51**, 1939–1953.

van der Kolk C.M., Guest W.S. and Potters J.H.H.M. 2001. The 3D shear experiment over the Natih field in Oman: the effect of fracture-filling fluids on shear propagation. *Geophysical Prospecting* **49**, 179–197.

Liu E., Hudson J.A. and Pointer T. 2000. Equivalent medium representation of fractured rock. *Journal of Geophysical Research* **105**(B2), 2981–3000.

Lucet N. 1989. *Vitesse et attenuation des ondes elastiques soniques et ultrasoniques dans les roches sous pression de confinement*. PhD thesis, University of Paris.

Mavko G. and Jizba D. 1991. Estimating the grain-scale fluid effects on velocity dispersion in rocks. *Geophysics* **56**, 1940–1949.

Mavko G. and Nur A. 1975. Melt squirt in the asthenosphere. *Journal of Geophysical Research* **80**, 1444–1448.

Murphy W.F. 1985. Sonic and ultrasonic velocities: Theory versus experiment. *Geophysical Research Letters* **12**, 85–88.

Nur A. 1971. Effects of stress on velocity anisotropy in rocks with cracks. *Journal of Geophysical Research* **8**, 2022–2034.

O'Connell R.J. and Budiansky B. 1977. Viscoelastic properties of fluid-saturated cracked solids. *Journal of Geophysical Research* **82**, 5719–5735.

Pointer T., Liu E. and Hudson J.A. 2000. Seismic wave propagation in cracked porous media. *Geophysical Journal International* **142**, 199–231.

Rathore J.S., Fjaer E., Holt R.M. and Renlie L. 1995. P- and S-wave anisotropy of a synthetic sandstone with controlled crack geometry. *Geophysical Prospecting* **43**, 711–728.

Schoenberg M. 1980. Elastic wave behavior across linear slip interfaces. *Journal of the Acoustical Society of America* **68**, 1516–1521.

Sothcott J., McCann C. and O'Hara S.G. 2000. The influence of two different pore fluids on the acoustic properties of reservoir sandstones at sonic and ultrasonic frequencies. 70th SEG Meeting, Calgary, Canada, Expanded Abstracts, 1883–1886.

Spencer J.W. 1981. Stress relaxation at low frequencies in fluid saturated rocks: attenuation and modulus dispersion. *Journal of Geophysical Research* **86**, 1803–1812.

Thomsen L. 1995. Elastic anisotropy due to aligned cracks in porous rock. *Geophysical Prospecting* **43**, 805–829.

Tod S.R. 2001. The effects on seismic waves of interconnected nearly aligned cracks. *Geophysical Journal International* **146**, 249–263.

Winkler K.W. 1985. Dispersion analysis of velocities and attenuation in Berea sandstone. *Journal of Geophysical Research* **90**, 6793–6800.

Zatsepin S.V. and Crampin S. 1997. Modelling the compliance of crustal rock, I. Response of shear-wave splitting to differential stress. *Geophysical Journal International* **129**, 477–494.